PAPER

Check for updates

Experimental and theoretical determination of the role of ions in atomic layer annealing†

Scott T. Ueda,[a] Aaron McLeod,[b] Youhwan Jo,[c] Zichen Zhang,[a] Jacob Spiegelman,[a] Jeff Spiegelman,[d] Dan Alvarez,[d] Daniel Moser,[e] Ravindra Kanjolia,[e] Mansour Moinpour,[e] Jacob Woodruff,[e] Kyeongjae Cho [iD][c] and Andrew C. Kummel [iD] *[b]

The atomic layer annealing process has recently shown promise as a technique for the deposition of crystalline materials that can be performed at the low temperatures of atomic layer deposition. However, the precise mechanism of the crystallization effect has not yet been thoroughly explored. In the present study, independent experimental control of ion momentum and energy are used in conjunction with molecular dynamics simulations to elucidate the role of ion energy and mass in atomic layer annealing. It was found that *via* a momentum transfer process, ions can displace surface atoms during initial contact and that they later induce a short-lived local heating phenomenon in the first few atomic layers, resulting in enhanced crystallinity. It was seen that by using a heavier gas such as Kr, energy transfer to the growth surface could be improved for AlN deposition, enabling the repair of a wider variety of crystallographic defects.

Introduction

As microelectronic devices continue to be scaled to the atomic limit, pressure on extant deposition methods such as physical vapor deposition (PVD) or conventional chemical vapor deposition (CVD) continues to increase. Increasingly stringent demands on thickness control, conformality, and material quality on the 3-dimensional (3-D) architectures commonly used in these devices has led to the greater adoption of atomic layer deposition (ALD) for thin film growth, especially in the low thermal budget back end of line.[1–6] Despite the numerous advantages of ALD, ALD-deposited films are often amorphous due to the moderate deposition temperatures (typically $< 400\ ^{\circ}$C) required to minimize precursor decomposition/desorption and to stay in the 'ALD window'.[4,7]

For many applications (*e.g.*, surface or bulk acoustic wave devices[8–11] or heat spreaders[12–14]), the deposition of crystalline films is required, which has led to the increasing adoption of a variant of ALD known as atomic layer annealing (ALA) as an

alternative or supplement to conventional plasma enhanced ALD (PEALD).[7,15–19] In the ALA process, either thermal ALD or PEALD is used to deposit the target material and low energy inert gas ions are used to bombard the surface. Using this ABC-type pulse sequence (reactant A, reactant B, and inert ions C), high-quality crystalline films can be deposited at low temperatures; however, the precise role of the inert ions in this process has thus far remained unclear.

In the present report, the mechanism of the ALA process is elucidated using AlN as an example material system due to its wide-ranging applications for crystalline films as a heat spreader or piezoelectric material. It was previously reported that ALA strongly relies on a so-called surface heating effect;[7,16,18,20] however, through systematic experimental variation of inert ion mass, plasma delay time, and molecular dynamics (MD) simulations, it is shown that the process is most consistent with a momentum transfer process resulting in effective local thermal excitation leading to surface crystallization (See schematic of ALA AlN process in Fig. 1).

Methods

Materials

Acetone (99.5+%), methanol (99.5+%), and deionized (DI) water (99.5+%) were purchased from Fisher Scientific. Hydrofluoric (HF) acid (48%) was purchased from VWR and diluted down to 2% with DI water before use. Tris(dimethylamido) aluminum

[a] *Materials Science and Engineering Program, University of California, San Diego, La Jolla, California 92093, USA*

[b] *Department of Chemistry and Biochemistry, University of California, San Diego, La Jolla, California 92093, USA. E-mail: akummel@ucsd.edu*

[c] *Department of Materials Science and Engineering, University of Texas at Dallas, Richardson, Texas 75080, USA*

[d] *Rasirc, Inc., San Diego, CA 92126, USA*

[e] *EMD Electronics, Haverhill, MA 01832, USA*

† Electronic supplementary information (ESI) available. See DOI: 10.1039/d1tc05194f

This journal is © The Royal Society of Chemistry 2022

J. Mater. Chem. C, 2022, **10**, 5707–5715 | 5707
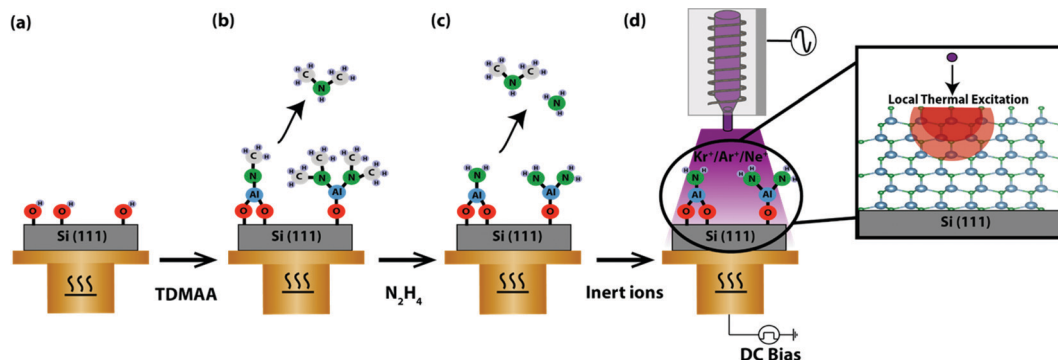
Fig. 1 Schematic Diagram of the ALA AlN Process. (a) Using hydroxyl-terminated Si as the starting substrate, (b) tris(dimethylamido) aluminum (TDMAA) dosing results in a surface terminated in aluminum dimethylamide and the release of dimethylamine gas. (c) Hydrazine (N_2H_4) dosing removes the surface bound dimethylamide as dimethylamine and ammonia gas. (d) The final step in the ALA process consists of low energy inert ion bombardment which induces crystallinity *via* a momentum transfer process that generates local thermal excitation (inset).

(TDMAA) was supplied by EMD performance materials. BRUTE anhydrous hydrazine was supplied by Rasirc, Inc. Ar (99.999+%) was purchased from Praxair and purified using an Entegris Gatekeeper gas purifier for use as a carrier gas for both TDMAA and hydrazine. Si(111) substrate wafers (Phosphorous, n-type) with a resistivity of 1–20 ohm cm were purchased from Waferworld. Research grade (99.999+%) Ne, Ar, and Kr gas purchased from Praxair was used as the plasma gas for the ALA process.

Sample preparation

Si(111) samples were first degreased using sequential 10 s rinses in acetone, methanol, and DI water. Following this degrease, the native Si oxide was removed *via* a cyclic HF clean consisting of sequential 1 min immersions in 2% HF solution and DI water for 2.5 cycles. Immediately following the cyclic HF clean, the samples were loaded onto a molybdenum sample holder and pumped down to a pressure of $< 2 \times 10^{-6}$ Torr before being loaded into the deposition chamber.

AlN deposition

AlN deposition conditions have been reported elsewhere.[19] Briefly, AlN deposition was conducted in a custom vacuum chamber (wall temp = 90 °C) with a base pressure $< 1 \times 10^{-6}$ Torr and consisted of a home-built reactor pumped by a dry pump (Edwards EPX 500NE) protected by both a liquid nitrogen cold trap and stainless steel mesh particle trap (see Fig. S1, ESI†). The sample stage consisted of a copper block heated externally *via* a cartridge heater and was electrically isolated to allow for biasing. Dosing was controlled using pneumatically actuated diaphragm valves and although self-saturating behavior was not observed, pulse times (100 ms for TDMAA and 150 ms for N_2H_4) and purge times (8 s for both precursors) were optimized for growth rates of ~0.9 Å per cycle to match typical ALD growth rates. TDMAA was dosed using a bottle temperature of 105 °C while N_2H_4 was kept at room temperature. Both the TDMAA and N_2H_4 cylinders were charged with Ar carrier gas to deliver the precursors to the sample. Gas flows were controlled by mass flow controllers and fed into a RF remote plasma source

(PIE Scientific) with a quartz plasma tube mounted above the chamber. ALA treatment time was fixed at 20 s (see optimization Fig. S2, ESI†) and used either Ne, Ar, or Kr gas at a pressure of 5 mTorr. The power was controlled to keep a constant ion current density of ~0.25 mA cm^{-2} (~1.5×10^{19} ions m^{-2} s^{-1}) in all cases.

X-ray photoelectron spectroscopy (XPS)

Chemical composition was determined *in vacuo* using an attached UHV chamber (Omicron VT, base pressure ~5×10^{-10} Torr). High resolution XP spectra were acquired on the as-deposited samples without any surface treatment (*e.g.*, Ar sputtering or UHV annealing) using a Mg Kα source ($h\nu = 1253.6$ eV) and DESA 150 electron analyzer (Staib Instruments) at a collection angle of 45° relative to the surface normal using a step width of 0.1 eV. Analysis of the XPS data was performed in CasaXPS v2.3 using Shirley background subtraction and Scofield photoionization cross sectional relative sensitivity factors.

X-Ray diffraction (XRD)

Ex situ grazing incidence X-ray diffractometry (GIXRD) was carried out on a Rigaku Smartlab diffractometer using a Cu Kα source ($\lambda = 0.154$ nm) operating at 40 kV. X-ray reflectivity (XRR) data was collected on the same tool with modeling and fitting conducted using the Smartlab Studio software suite (Rigaku). For consistency, all samples were of approximately the same thickness of ~40 nm as measured by XRR.

Atomic force microscopy (AFM)

Sample topography was determined using a Keysight 5500 scanning probe microscope in tapping mode using, etched Si tips with Al backside coating (Bruker).

Electrical characterization

Capacitance–Voltage (*C–V*) and current–voltage (*I–V*) spectroscopy was perfomed using a capacitor structure fabricated using standard techniques. Briefly, the dielectric films on Si substrate underwent top gate electrode deposition *via* thermal

5708 | *J. Mater. Chem. C*, 2022, **10**, 5707–5715

This journal is © The Royal Society of Chemistry 2022
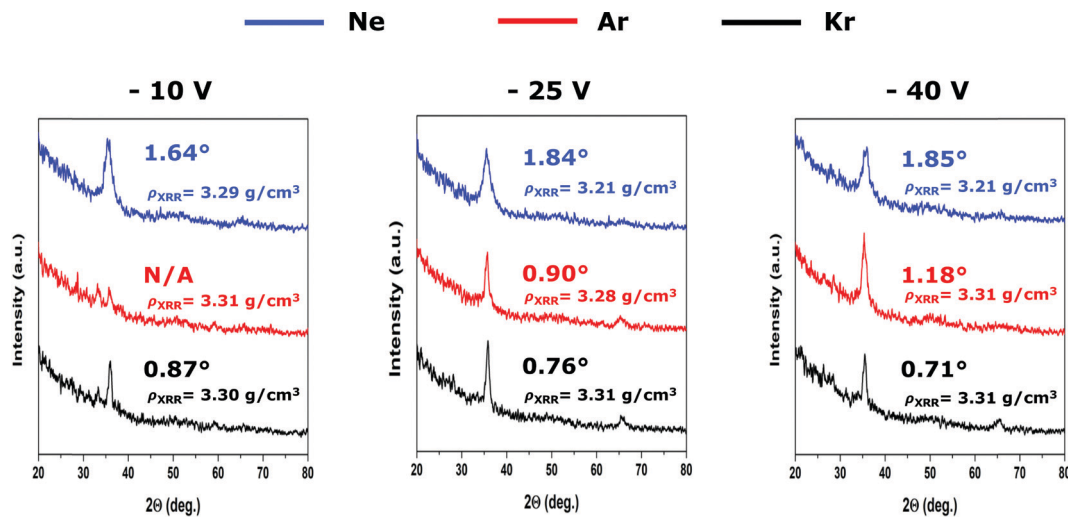
Fig. 2 GIXRD data comparing ALA AlN films using Ne, Ar, or Kr gas at various bias voltages. Using the FWHM of the AlN (002) peak as a metric for crystallinity, Kr can be seen to result in the highest quality crystalline films over a wide range in energy. At -25 V and -40 V bias, crystallinity can be seen to scale with ion mass consistent with the momentum transfer hypothesis. Note: Treatment time for all samples was fixed at 20 s while ion current density was maintained at a constant ~ 0.25 mA cm^{-2} ($\sim 1.5 \times 10^{19}$ ions m^{-2} s^{-1}) for all conditions. All samples were approximately the same thickness of ~ 40 nm as measured by XRR. All samples had near bulk density consistent with a very low fraction of amorphous material.

evaporation (Denton 502) consisting on a 50 nm layer of Ni, with the geometry defined using a shadow mask. A blanket Ti/Au backside ohmic contact was then deposited using sputter deposition (Denton 18). I–V and multi-frequency C–V characterization was carried out in the range of 20 kHz to 1 Mhz on a Keithley 4200A parameter analyzer. Post-deposition forming gas anneal (FGA) was performed after initial electrical characterization on a AW610 rapid thermal anneal system and consisted of a 15 minute anneal at 400 °C in an atmosphere of 5% H_2 in N_2.

Results and discussion

To determine the effect of ion momentum and energy on the ALA process, various inert gasses were used for the ion treatment step in addition to a controlled DC bias applied to the substrate. By changing the inert gas from Ne (~ 20 amu) to Ar (~ 40 amu) or Kr (~ 80 amu), while maintaining constant ion current density and treatment time, momentum could independently be tuned from energy and flux. If the primary crystallization effect was due to a plasma heating effect, it was expected that the crystallization effect would be independent of inert ion mass, or as noted in previous reports,[16,21] that heavier ions would reduce the crystalline quality of the film by inducing ion damage.[18,22]

As it can be seen in the GIXRD scans in Fig. 2, the full width at half maximum (FWHM) of the AlN (002) GIXRD peaks in general decreased with increasing ion mass, with Kr exhibiting the lowest FWHM and therefore the best crystallinity over a range of energy from −10 V to −40 V. The ideal case for epitaxial film growth is when a non-penetrating ion impacts the surface with enough energy to stimulate surface atom displacement/diffusion while minimizing that effect in the

bulk[23–25] which makes heavy/large inert gasses like Kr ideal for AlN. C–V/I–V electrical characterization carried out on the three samples deposited at the −40 V condition was largely in agreement with the GIXRD data, with the sample deposited using Kr possessing the lowest defect density and the sample deposited using Ne containing the highest defect density (Fig. S3 and S4, ESI†).

As shown below in MD simulations, gasses with small atomic radii like Ne can penetrate into the AlN film and cause detrimental effects on crystallinity whereas Kr is much less prone to this while also being able to transfer large quantities of momentum at low energy owing to its large atomic mass. However, at very low bias energy, the use of Ne resulted in more effective crystallization than Ar. It is possible that this is due to the much higher ionization energy of Ne (21.6 eV) as compared to Ar (15.8 eV) and that at low kinetic energy, the potential energy imparted on the film as a result of neutralization of the Ne ions[23] (thermal energy of ~ 17.1 eV including AlN charge neutrality level of ~ 4.5 eV)[26] is the dominant effect whereas at higher kinetic energy (bias), momentum transfer induced collision cascades become the dominant factor. At −10 V, Ar ions do not have enough potential energy (compared to Ne ion) nor momentum transfer (compared to Kr), leading to poor crystallization of growing AlN films as shown in the left panel of Fig. 2.

AFM was used to verify the surface morphology of the films and as it can be seen in Fig. 3, all films were smooth, with sub-nm roughness that was nearly identical irrespective of the inert gas used for the ALA plasma treatment. The lack of damage from heavy ions is likely attributable to the low ion energies involved in the process as a result of the substrate biasing, which is a technique extensively used in PEALD to control ion energy and tailor material growth properties.[27,28] Therefore, it can be concluded at low energy, the potentially detrimental
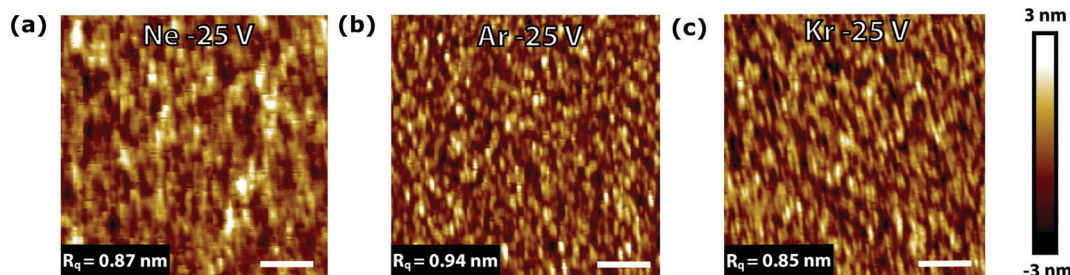
Fig. 3 AFM data comparing effect inert gas used during ALA. At a constant bias of -25 V, AFM data show RMS surface roughness (R_q) is relatively unchanged when using (a) Ne, (b) Ar, or (c) Kr as the gas in the ALA process with all cases displaying sub-nm roughness. Scale bar, 500 nm.
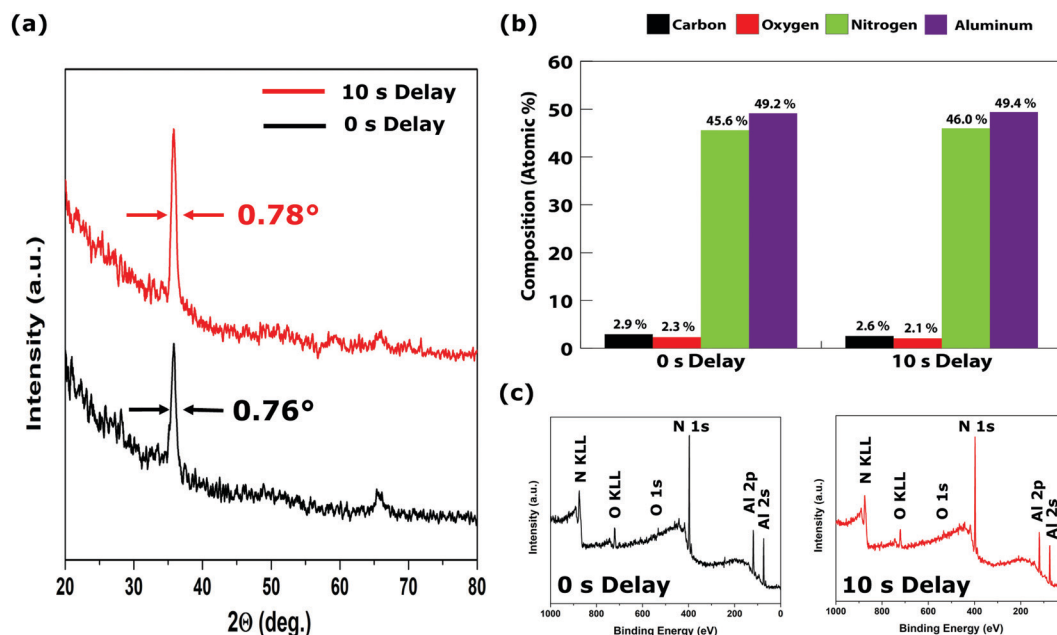
Fig. 4 GIXRD and XPS comparing effect of ALA delay time on crystallinity. (a) As compared to using a 0 s delay (instant) between the ALA plasma treatment step and the subsequent organometallic pulse, using a delay of 10 s results in no reduction in AlN crystalline quality in GIXRD as measured by both signal intensity as well as FWHM. (b and c) XPS chemical composition data are nearly identical for 0 s and 10 s delay.

effects of ion bombardment by heavy gasses may be mitigated and that a heavy inert gas such as Kr may successfully be used for the ALA deposition of a smooth and highly crystalline AlN film.

To further confirm the momentum transfer hypothesis, the effect of delay time between the ion treatment step and the TDMAA pulse was studied using Kr gas at −25 V stage bias. It has been previously reported that the delay between the ALA plasma treatment step and the following reactant pulse must be minimized to achieve the best crystallinity due to a surface heating effect; however, as seen in Fig. 4a, the crystallinity as determined by both signal intensity as well as FWHM of the AlN (002) peak is relatively unchanged from a 0 s delay to a 10 s delay. This is to be somewhat expected as many other previous reports on ion-irradiated solids have reported the "thermal spike" phase is usually on the order of 10^{-11}–10^{-12} s[23,29] as opposed to the 10^0 s timescales seen in other ALA reports using PEALD followed by inert gas ion treatment.[7,18,20] It is hypothesized that

the apparent time dependence of crystallinity seen by others is due to partial surface oxidation or some other form of surface contamination that occurs during the delay and interferes with crystallinity.[30]

XPS was used to probe chemical composition of the two samples and as shown in Fig. 4b and c, XPS data of the samples with 0 s delay and 10 s delay have nearly identical, low O and C contamination and virtually identical chemical shift data that are consistent with the formation of AlN (Fig. S5, ESI†). Through the use of a high vacuum ALD system which included a liquid nitrogen cold trap to minimize background H_2O, film contamination was minimized even when using a 10 s delay and consistent with crystallinity being relatively unchanged irrespective of delay time, in agreement with the collision cascade hypothesis.

As a final experimental verification of the idea of ion induced collision cascades, the ALA treatment was performed every cycle, every other cycle, and every third cycle. As it can be
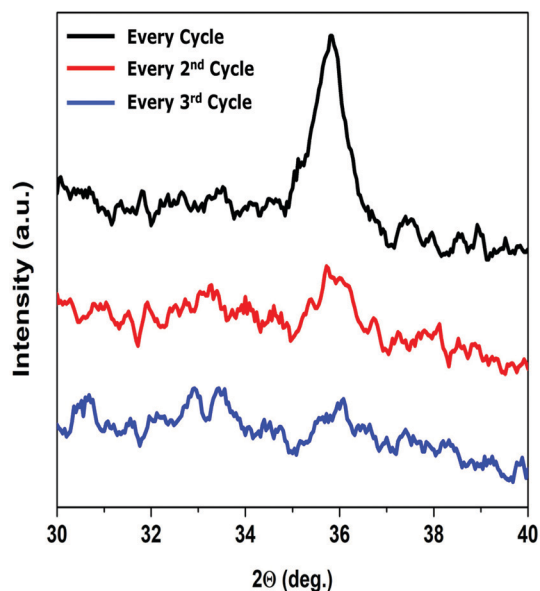
Fig. 5 GIXRD data comparing effect of cycles per ALA treatment. Crystallinity is seen to rapidly decrease as a function of cycles per ALA treatment. When performed every cycle, crystallinity is strong (black), while the AlN (002) peak is barely above signal-to-noise when performing ALA every other cycle (red). Performing ALA every third cycle results in no detectable crystallinity (blue).

seen in Fig. 5, crystallinity rapidly fell off when dosing ions in every other cycle or every third cycle. This is consistent with ion induced crystallinity being confined to the first and second atomic layers and being extremely localized. If a heating effect

on the order of ~1 s was largely responsible for the crystallization effect, it is unlikely to be confined to only the first monolayer of the surface;[31] therefore, the data are much more consistent with the low energy incident ions transferring energy primarily to the top atomic layer of the growth surface which is then being dissipated via phonon transport in a short-lived process that acts as a localized thermal excitation.

To validate the experimental work and gain a deeper understanding of the ion–AlN interaction, classical molecular dynamics (MD) was used to investigate the ALA crystallization effect using Kr and Ne ions (the heaviest and lightest species tested experimentally). As shown schematically in Fig. 6a, the simulation involved a single inert gas atom with 40 eV energy colliding with an AlN structure composed of 1–2 monolayers of disordered AlN atop a perfectly crystalline AlN (002) slab. This structure was used to simulate the amorphous or defective layer of AlN that results from the thermal AlN ALD before the ALA treatment is performed. The disordered layer contained irregularities such as voids and two distinct types of defects that are shown schematically in Fig. 6b and c. The first defect was an interstitial Al point defect (hereafter referred to as defect 'A') and the second was a N point defect (hereafter referred to as defect 'B') that was part of a larger non-crystalline atomic chain.

Briefly summarizing the simulation details, the Vashishta potential[32] was used for AlN, and the interactions between inert gas atoms and AlN were described by the Lennard-Jones (LJ) potential. Parameter values for the LJ potential were determined using the Waldman–Hagler mixing rule[33] and listed in Table S1 (ESI†). To ensure simulations were accurate and realistic, the microcanonical ensemble was used with the
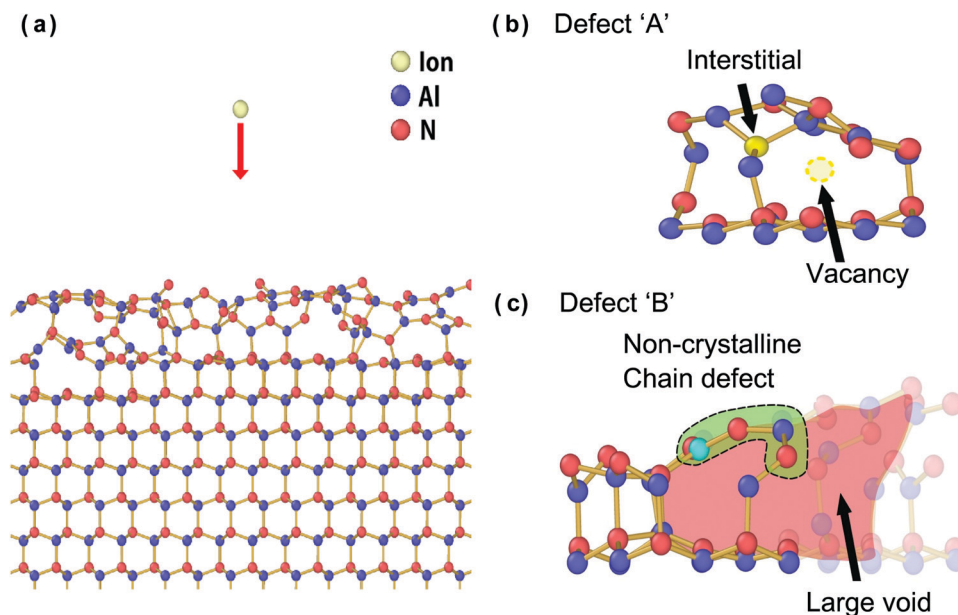
Fig. 6 Schematic diagram of ion impact simulation. (a) The simulation consisted of a single 40 eV inert gas ion colliding with an AlN surface comprised of a disordered layer atop a crystalline AlN (002) slab. The disordered layer contains voids and defects to simulate the AlN film before ALA treatment. (b) The first defect included in the simulation (defect 'A') is a Frenkel defect generated by an interstitial Al atom (yellow). The interstitial generated an Al vacancy depicted as a hollow yellow circle. (c) The second defect in the simulation (defect 'B') is a larger, non-crystalline atomic chain defect shown representatively as a N point defect (turquoise) for ease of viewing. The point defect is just one of the atoms in a non-crystalline position.

This journal is © The Royal Society of Chemistry 2022

J. Mater. Chem. C, 2022, 10, 5707–5715 | 5711
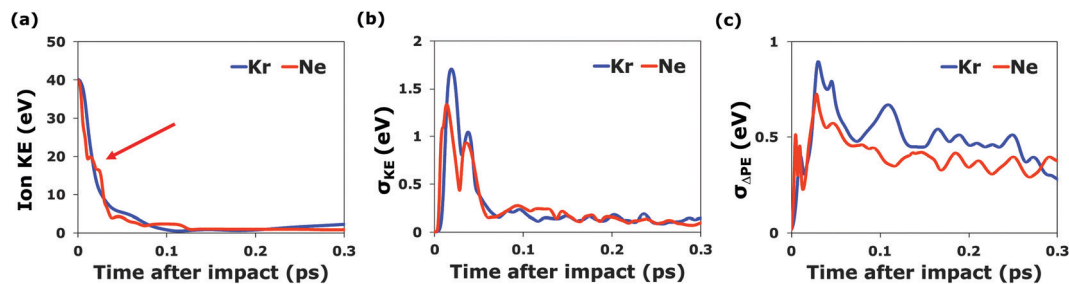
Fig. 7 Simulation results during initial contact phase of ion collision. (a) During initial contact with AlN, both Kr (blue) and Ne (red) show similar kinetic energy profiles which show the transfer of energy to AlN occurred over a timescale of ∼0.1 ps; however, a non-monotonic decrease in Ne kinetic energy was seen due to the atom undergoing multiple sequential collisions (b) the local standard deviation of kinetic energy (σ_{KE}) of AlN atoms nearby the impact site is greater in the first collision (peak at ∼0.01 ps) in the case of Kr because the Kr has a higher energy loss per unit length, leading to a more intense and more localized energy transfer to AlN. (c) The standard deviation of the change in potential energy of AlN ($\sigma_{\Delta PE}$) is greater in the case of Kr due to the multiple, sequential collisions generated by Ne generating a more diffuse surface heating as compared to the singular impact in the case of Kr.
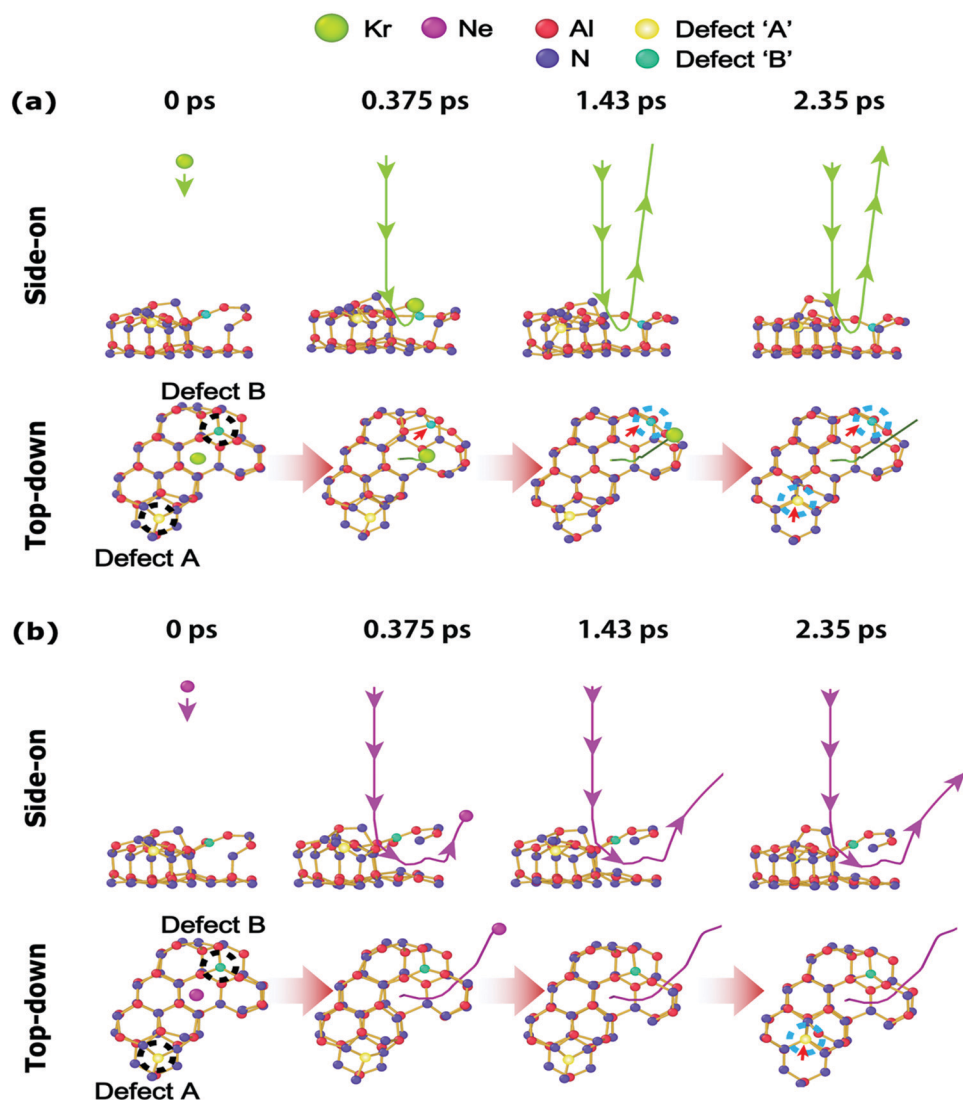
Fig. 8 MD simulation of the local structure relaxation of AlN with an impinging atom. Atoms are color-coded with respect to atomic species except for the two defects. The solid lines are the trajectories of the impinging inert gas atoms. Defects are circled in cyan if they are repaired during the collision cascade. (a) The Kr ion is shown to not penetrate into the bulk of the film and results in the annihilation of defect 'B' within < 1 ps of ion impact and the repair of defect 'A' after several ps (b) the Ne ion is shown to penetrate further into the AlN film while also being unable to repair or remove defect 'B' though the surface heating effect was still able to remove defect 'A' after ∼ 2 ps. The full collision simulation is shown in supplementary video 1 and 2.

timestep size selected to limit the displacement of an atom per step to 0.05 Å. All simulations were performed using LAMMPS[34] at an initial temperature of 0 K with visualizations generated using OVITO.[35] In order to generate descriptive statistics regarding the defect healing, 49 distinct ion trajectories were modeled in a rectilinear grid around defect 'B' and the healing of both defects "A" and "B" was objectively assessed by comparing the atomic bonding vector of the defective site relative to the ideal crystallographic position.

Based on the simulation results, two distinct interaction stages were found following the impact of an inert gas ion: the initial contact and final relaxation stages. During the initial contact stage, the incident ion quickly transfers its energy into the AlN over a period of $\sim$0.1 ps (Fig. 7a) and although the timescale over which this energy transfer occurred was similar for both Kr and Ne, qualitative and quantitative differences were noted. Whereas the Kr ion collision occurred as essentially a singular collision (owing to its higher momentum and/or larger atomic radius), the Ne atom underwent several sequential collisions (see non-monotonic decrease in energy for Ne in Fig. 7a), leading to a lower energy transfer per unit ion path length. This effect can be understood as stemming from the high elastic modulus of AlN ($\sim$500 GPa[36]), where a large force is needed to deform the surface. Because force is proportional to momentum, the higher mass Kr ion was able to deform the AlN surface and transfer a high amount of energy to a very localized area whereas the lighter Ne ion generated only a minor deformation before being deflected.

Although macroscopic energy transfer in the case of both Kr and Ne was similar, the use of Kr ions resulted in a more localized and more intense change in the potential and kinetic energy of the growing AlN film because unlike Ne atoms, Kr atoms did not undergo multiple, sequential collisions. This difference was quantified by comparing the local standard deviation of kinetic energy (σ_{KE}) and the local standard deviation of the change in potential energy of AlN ($\sigma_{\Delta PE}$) of AlN

atoms nearby the impact site (Fig. 7b and c). The higher σ_{KE} measured in the case of Kr indicated more concentrated energy transfer to the AlN surface which could remove complex defects while the higher $\sigma_{\Delta PE}$ indicated the Kr ion generated a more localized and more intense heating effect.

In contrast to the fast initial contact stage, the relaxation stage occurs over longer timescales (several ps) corresponding to the "thermal spike" phase of ion-irradiated solids. It is during this stage that the local structure of AlN can be thermally relaxed using energy transferred from an impinging atom. In the cases of both Kr (Fig. 8a) and Ne (Fig. 8b), *defect 'A' is repaired* during the relaxation stage as the defects received enough thermal energy to move into a crystalline site by surface heating; however, *defect 'B' was removed only in the case of Kr* because of the higher local energy required to remove the entire defect chain. Although the total amount of energy transferred is similar in the case of both Ne and Kr, the crystallization effect seen both experimentally and in simulations was stronger in the case of Kr, owing to the larger local momentum transfer of the Kr ion. It is also noted that owing to the larger atomic radius of Kr, the penetration depth of Kr is also much shallower as compared to Ne, which would reduce embedded species or the generation of defects in the bulk of the film.

To confirm a statistically significant difference in the healing behavior of Kr and Ne, 49 distinct ion impacts were modeled for each gas. As it can be seen in Fig. 9a below, ion impacts sites were chosen to be uniformly distributed around point defect B, though direct ion–atom collisions were avoided because they were assumed to be extremely uncommon. After simulations were conducted, the post-collision position of both defect A and B were analyzed based on atomic bonding vector and assigned a binary value of healed or unhealed (Fig. 9b). The allowance from the ideal bond angle and length used to assign the defects as healed or unhealed was incremented in steps of 5–10% and kept to the minimum amount needed to generate at least 30 healed defects (to properly compare the healing rates of
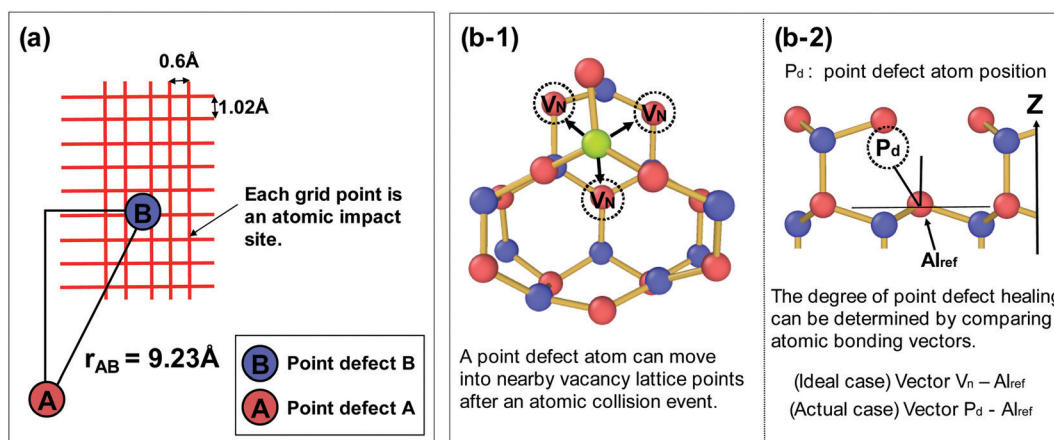
Fig. 9 Experimental methodology for the simulation of ion impact with defective AlN surface. (a) collision impact points are uniformly distributed nearby defect B, with x and y grid spacing selected to avoid head-on collisions which are assumed to be extremely uncommon. (b) Based on the post-collision position of a point defect, it is possible to decide whether a point defect is healed or not based on the atomic bonding vector.
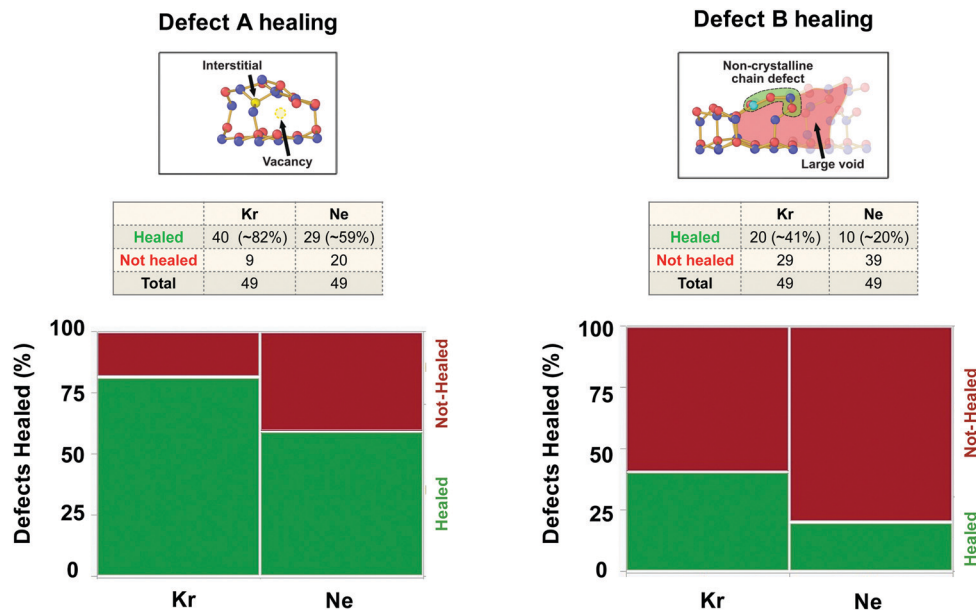
Fig. 10 Full results of 49 simulations run for each Kr and Ne ion bombardment on a defective AlN surface in terms of defect A and defect B healing. Point defect A is Frenkel defect that can be repaired *via* bond exchange and requires much less energy to heal as compared to defect B (the atomic chain defect), which requires bond breaking to repair. This higher energy needed to repair defect B is reflected in the lower overall healing rate, though it is noted that in the cases of both defect A and defect B, Kr is more effective than Ne.

each gas). Though the tolerance chosen does affect results somewhat, it is noted that regardless of the values chosen, the percentage of defects healed using Kr gas was always higher than the percentage healed using Ne. It is also noted that this binary classification is specific to the point defects being studied and not of the structure as a whole.

Results from the simulation (Fig. 10) were compared using Fisher's exact test, using a 0.05 level of significance. In the case of defect A, Kr was determined to be more effective at healing as compared to Ne ($p = 0.026$) and in the case of defect B, Kr was again determined to be more effective ($p = 0.047$).

The results of the simulation were in good agreement not only with the experimental data, but also with other ion–solid collision simulations modeling with the timescales over which the surface heating effect was expected to occur.[23,31] Furthermore, the crystallization effect was shown both experimentally and in simulations of this work to depend on the inert gas used to bombard the growth surface: Kr was shown be more effective than Ne due to higher energy transfer to the surface and lower penetration depth leading to effective defect healing in the crystallization of ALD-grown amorphous layers on the bulk crystalline film.

Conclusion

In summary, it is demonstrated that the key mechanism of atomic layer annealing is a momentum transfer process where the incoming ions can remove defects both during the initial collision with the growing film and also during the later thermal relaxation stage where lattice vibrations act as local thermal excitation. Kr gas is shown experimentally to result in

higher crystallinity as measured *via* a smaller FWHM in GIXRD, and MD simulations confirm at a statistically significant level that Kr ions are more effective at defect repair when compared to a lighter inert gas due to its larger and more localized momentum transfer to the growth surface. Furthermore, through the use of modest substrate biasing, it is shown that heavier ions (*e.g.*, Kr) can successfully be used without introducing surface damage. By varying the time delay after ALA treatment together with XPS and GIXRD measurements, it is demonstrated that the local heating effect is extremely short lived and MD simulations are used to further reinforce this conclusion.

Author contributions

Scott T. Ueda: experimental methodology, investigation, data visualization, formal data analysis, and writing. Aaron McLeod: investigation and formal analysis. Youhwan Jo: investigation, formal analysis, and writing. Zichen Zhang: investigation. Jacob Spiegelman: investigation. Jeff Spiegelman and Dan Alvarez: resources—provision of the anhydrous hydrazine source and related technical expertise on installation and use. Daniel Moser, Ravindra Kanjolia, Mansour Moinpour, and Jacob Woodruff: resources—synthesis and provision of the TDMAA precursor and related technical expertise on its use. Kyeongjae Cho: supervision. Andrew C. Kummel: experimental conceptualization, project administration and supervision.

Conflicts of interest

The authors declare no competing financial interests.

5714 | *J. Mater. Chem. C*, 2022, **10**, 5707–5715

This journal is © The Royal Society of Chemistry 2022

Acknowledgements

References

1 I. Ferain, C. A. Colinge and J. P. Colinge, *Nature*, 2011, **479**, 310–316.

2 M. Fang and J. C. Ho, *ACS Nano*, 2015, **9**, 8651–8654.

3 M. Leskelä and M. Ritala, *Angew. Chem., Int. Ed.*, 2003, **42**, 5548–5554.

4 R. W. Johnson, A. Hultqvist and S. F. Bent, *Mater. Today*, 2014, **17**, 236–246.

5 P. O. Oviroh, R. Akbarzadeh, D. Pan, R. A. M. Coetzee and T. C. Jen, *Sci. Technol. Adv. Mater.*, 2019, **20**, 465–496.

6 R. A. Ovanesyan, E. A. Filatova, S. D. Elliott, D. M. Hausmann, D. C. Smith and S. Agarwal, *J. Vac. Sci. Technol., A*, 2019, **37**, 060904.

7 H. Y. Shih, W. H. Lee, W. C. Kao, Y. C. Chuang, R. M. Lin, H. C. Lin, M. Shiojiri and M. J. Chen, *Sci. Rep.*, 2017, **7**, 39717.

8 M. Clement, L. Vergara, J. Sangrador, E. Iborra and A. Sanz-Hervás, *Ultrasonics*, 2004, **42**, 403–407.

9 H. P. Loebl, M. Klee, C. Metzmacher, W. Brand, R. Milsom and P. Lok, *Mater. Chem. Phys.*, 2003, **79**, 143–146.

10 K. Umeda, H. Kawamura, M. Takeuchi and Y. Yoshino, *Vacuum*, 2008, **83**, 672–674.

11 M. Gillinger, K. Shaposhnikov, T. Knobloch, M. Stöger-Pollach, W. Artner, K. Hradil, M. Schneider, M. Kaltenbacher and U. Schmid, *Appl. Surf. Sci.*, 2018, **435**, 432–437.

12 R. L. Xu, M. Munõz Rojo, S. M. Islam, A. Sood, B. Vareskic, A. Katre, N. Mingo, K. E. Goodson, H. G. Xing, D. Jena and E. Pop, *J. Appl. Phys.*, 2019, **126**, 185105.

13 C. Duquenne, M. P. Besland, P. Y. Tessier, E. Gautron, Y. Scudeller and D. Averty, *J. Phys. D: Appl. Phys.*, 2012, **45**, 015301.

14 Y. Bian, M. Liu, G. Ke, Y. Chen, J. DiBattista, E. Chan and Y. Yang, *Surf. Coat. Technol.*, 2015, **267**, 65–69.

15 S. H. Yi, K. W. Huang, H. C. Lin and M. J. Chen, *J. Mater. Chem. C*, 2020, **8**, 3669–3677.

16 W. C. Kao, W. H. Lee, S. H. Yi, T. H. Shen, H. C. Lin and M. J. Chen, *RSC Adv.*, 2019, **9**, 12226–12231.

17 H. Seppänen, I. Kim, J. Etula, E. Ubyivovk, A. Bouravleuv and H. Lipsanen, *Materials*, 2019, **12**, 406.

18 W. H. Lee, Y. T. Yin, P. H. Cheng, J. J. Shyue, M. Shiojiri, H. C. Lin and M. J. Chen, *ACS Sustainable Chem. Eng.*, 2019, **7**, 487–495.

19 S. T. Ueda, A. McLeod, D. Alvarez, D. Moser, R. Kanjolia, M. Moinpour, J. Woodruff and A. C. Kummel, *Appl. Surf. Sci.*, 2021, **554**, 149656.

20 W. H. Lee, W. C. Kao, Y. T. Yin, S. H. Yi, K. W. Huang, H. C. Lin and M. J. Chen, *Appl. Surf. Sci.*, 2020, **525**, 146615.

21 X. A. Cao, S. J. Pearton, A. P. Zhang, G. T. Dang, F. Ren, R. J. Shul, L. Zhang, R. Hickman and J. M. Van Hove, *Appl. Phys. Lett.*, 1999, **75**, 2569–2571.

22 J. P. Holgado, A. Barranco, F. Yubero, J. P. Espinos and A. R. González-Elipe, *Nucl. Instrum. Methods Phys. Res., Sect. B*, 2002, **187**, 465–474.

23 A. Anders, *Thin Solid Films*, 2010, **518**, 4087–4090.

24 D. K. Brice, J. Y. Tsao and S. T. Picraux, *Nucl. Instrum. Methods Phys. Res., Sect. B*, 1989, **44**, 68–78.

25 G. Carter, *Phys. Rev. B: Condens. Matter Mater. Phys.*, 2000, **62**, 8376–8390.

26 V. N. Brudnyi, *Russ. Phys. J.*, 2017, **59**, 2186–2190.

27 H. B. Profijt, M. C. M. Van De Sanden and W. M. M. Kessels, *Electrochem. Solid-State Lett.*, 2012, **15**, G1–G3.

28 H. B. Profijt, M. C. M. van de Sanden and W. M. M. Kessels, *J. Vac. Sci. Technol., A*, 2013, **31**, 01A106.

29 J. C. Liu, J. Li and J. W. Mayer, *J. Appl. Phys.*, 1990, **67**, 2354.

30 V. Brien and P. Pigeat, *J. Cryst. Growth*, 2008, **310**, 3890–3895.

31 H. A. Atwater, C. V. Thompson and H. I. Smith, *J. Appl. Phys.*, 1988, **64**, 2337.

32 P. Vashishta, R. K. Kalia, A. Nakano and J. P. Rino, *J. Appl. Phys.*, 2011, **109**, 033514.

33 M. Waldman and A. T. Hagler, *J. Comput. Chem.*, 1993, **14**, 1077–1084.

34 S. Plimpton, *J. Comput. Phys.*, 1995, **117**, 1–19.

35 A. Stukowski, *Modell. Simul. Mater. Sci. Eng.*, 2010, **18**, 015012.

36 Y. Lu, M. Reusch, N. Kurz, A. Ding, T. Christoph, M. Prescher, L. Kirste, O. Ambacher and A. Žukauskaitė, *APL Mater.*, 2018, **6**, 076105.

This journal is © The Royal Society of Chemistry 2022

J. Mater. Chem. C, 2022, **10**, 5707–5715 | **5715**